Reconfigurable Origami-Inspired Metamaterials for Controllable Sound Manipulation

Yifan Zhu, Fan Fei, Shiwang Fan, Liyun Cao, Krupali Donda, and Badreddine Assouar

Design and experimental demonstration of reconfigurable origami-inspired metamaterials for controllable sound manipulation

Yifan Zhu[*], Fan Fei, Shiwang Fan, Liyun Cao, Krupali Donda, and Badreddine Assouar[*]

Institut Jean Lamour, CNRS, Université de Lorraine, F-54000 Nancy, France.

Abstract

Creating complex spatial objects from a flat sheet of material using origami folding techniques has attracted attention in science and engineering. Here, we design, model and fabricate reconfigurable origami-inspired metamaterials whose unit cells can be easily tailored into numerous specific shapes. Via combinations of different shapes of the unit cell in the metamaterial panel, we numerically and experimentally demonstrate various specific sound wave manipulations, including acoustic focusing, beam splitting, sound localization, and one-way transmission. Our design features simple configuration, tunable structure, multiple functionalities, and light weight. This finding provides a new route for controllable sound manipulation, paving the way towards reconfigurable functional meta-device based on origami-inspired metamaterials.

Keywords: Origami-inspired, Metamaterials, Reconfigurable, Sound manipulation, Multifunctionality.

Corresponding authors:

*yifan.zhu@univ-lorraine.fr

*badreddine.assouar@univ-lorraine.fr

I. INTRODUCTION

Origami [1-2] is the ancient art of paper folding, which has received great attentions in science and engineering. Recently, origami has been widely used in mechanical metamaterial designs [3], providing various extraordinary properties, such as abnormal Poisson's ratios [4-10], topological mechanical phase [11], and reprogrammable designs [12-13]. On the other hand, origami has been also applied in other science and engineering fields, such as robots [14-15], battery fabrication [16], thermal devices [17], nanocomposites [18], and architecture designs [19], showing the great application potential of the origami folding techniques in different domains.

Very recently, actuated origami-inspired transformable metamaterials were proposed [20]. They have been extended to the design of reconfigurable acoustic waveguide [21], in which general acoustic wave propagation and radiation fields are measured. However, up to now, the origami folding method for specific sound wave manipulation and beam shaping [22-24] has not been explored or investigated.

In this research, we explore and demonstrate various sound wave manipulations by designing reconfigurable origami-inspired metamaterials (ROIM). The origami-based unit cells are made by hardboard, which can be actively deformed into numerous specific shapes. A tunable and multifunctional metamaterial panel is therefore fabricated with reconfigurable origami-based unit cells. Via combinations of different shapes of the unit cells, we numerically and experimentally demonstrate acoustic focusing [25], beam splitting [26], localization [27] and one-way transmission [28]. Our design features simple configuration, tunable structure, multiple functionalities, and light weight. Our findings could potentially open a new avenue towards reconfigurable and tunable functional acoustic device based on origami approach, and may lead to various practical applications, such as noise and sound field control.

II. UNIT CELL DESIGN

The designed ROIM is made up of reconfigurable origami-based unit cell, which is schematically shown in Fig. 1. The fabrication processes including folding, cutting and pasting [20] are illustrated in Fig. 1(a). The origami-based unit cell is made from a flat hardboard. Figures 1(b-d) show the samples and the schematic diagrams of the three-dimensional (3D) and two-dimensional (2D) reconfigurable unit cell with four specific shapes (denoted as States #0-3). State #1 has a channel shape as shown in the figure. The width and the length of the channel are a=2cm, and b=6cm, respectively. There are two tunable sheets (blue parts) on the both sides of the channel which can be rotated with specific angles (α_1-α_4, as marked in Fig. 1(d)). State #1 has α_1=α_2=90°, and α_3=α_4=0° with 2 exits. State #2 has α_1=α_2=α_3=α_4=90° with a pair of 2D crossed channels with 4 exits. State #3 has α_1=α_3=0°, α_2=α_4=90° (or α_1=α_3=90°, α_2=α_4=0°) with 3 exits, while State #0 (or denoted as folded) is obtained by folding the z-direction-vertical structure State #1-3 (β=90°) into a flat sheet (β=0°). The above four states of the unit cell can be easily deformed by changing the parameters of α_1-α_4 and β. We will show later that these different states have unique functionalities in sound manipulation. The schematic diagram of the reconfigurable metamaterial panel consist of unit cells with different states is shown in Fig. 1(e). The parameters of angles are marked in the figure.
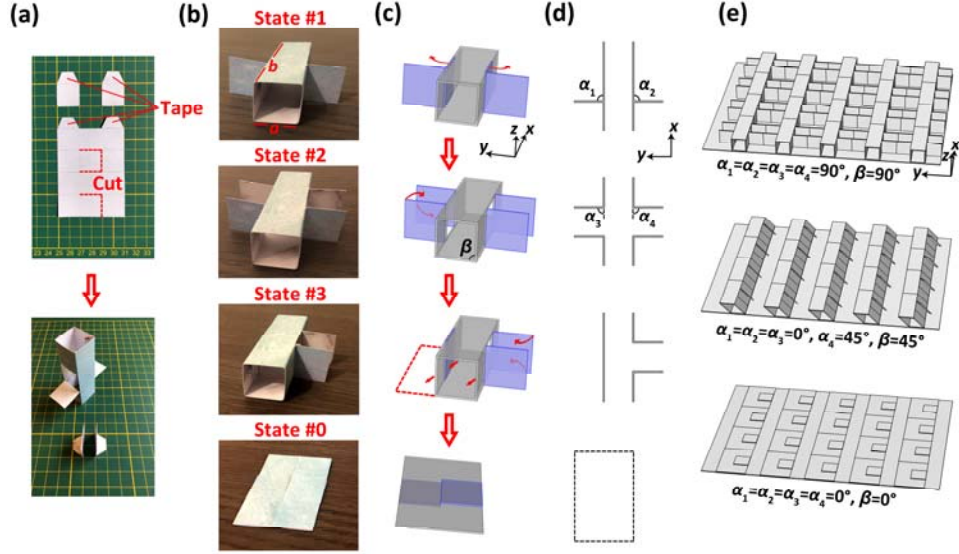
FIG. 1. (a) The fabrication process of origami unit cell including folding, cutting and pasting, which is made from a flat hardboard. (b) Photographs of the origami samples of the unit cell. Four different shapes are denoted as State #1, State #2, State #3, and State #0, respectively. (c) The 3D schematic diagram of the reconfigurable unit cells. (d) The 2D schematic diagram of the reconfigurable unit cells. The unit cell can be actively deformed by changing the parameters of α_1-α_4 and β. (e) The schematic diagram of the reconfigurable metamaterial panel. The parameters of angles are marked in the figure.

III. SOUND MANIPULATIONS

A. Acoustic focusing

Based on the origami structures illustrated in Fig. 1, we have investigated different functionalities associated to sound wave manipulation, to evidence the outstanding capabilities of these metamaterials for steering sound waves with simple and reconfigurable structures. We, first, start with the acoustic focusing [25] functionality making use of these designed materials. Figure 2 shows the realizations of acoustic focusing by RIOM. The arrangement of the array consists of

4×5 unit cells. The number "0" and "1" represent State #0 and State #1 of the unit cells. Since the designed array has single layer, it can be effectively characterized as a 2D model as shown in Fig. 2(b). The arrows indicate the incident and the transmitted directions of the waves. They are incident from the opening of the middle unit cell at the left interface. Figure 2(c) shows the photograph of the metamaterial panel sample. A unit cell can cover a space of 6cm×6cm×2cm. 4×5 unit cells are fixed on a plate with the size of 24cm×32cm. Here, the configuration of State #1 can effectively guide the acoustic wave in *x*-direction. State #0 is a folded planar sheet as a defect in the array filled with background medium air. We use the phase shift difference between the narrow channels formed by States #1 and the cavities formed by States #0 to manipulate the acoustic wavefront at outside interface (see details in Appendix A). Based on Fermat principle [25], the required phase distribution in *y*-direction is:

$$\phi = k(\sqrt{x_0^2 + (y - y_0)^2} - \sqrt{x_0^2 + y_0}), \tag{1}$$

where $k=2\pi f/c_0$ is the wave number, c_0 is sound speed in air, and (x_0, y_0) is the focal coordinate. In order to design the focal point at 10cm away from the interface, the phase distribution is $\phi = k(\sqrt{y_0^2 + 0.01} - 0.1)$ as shown in Fig. 2(d). The unit cells marked by 1-5 in Fig. 2(c) can mimic the discrete phase profile shown in Fig. 2(d) to realize acoustic focusing.

To evidence the capability of the tailored origami metamaterial, illustrated in Figs. 2(a-d), and its specific designed functionality, we have carried out numerical and experimental investigations. In this work, the simulations were done by COMSOL Multiphysics 5.4a. The considered density and the sound speed of air are $\rho_0=1.21$kg/m^3 and $c_0=343$m/s, respectively. The density and the sound speed of the hardboard are $\rho_1=1200$kg/m^3 and $c_1=500$m/s, respectively. Here, in the simulations, the hardboard is simplified as an acoustic medium. The simulation results are similar when it is considered as an elastic medium or hard boundary (see Appendix B).

The experiments were carried out in 2D parallel waveguide experimental system (1.8m×1m) [29]. The distance between two parallel waveguides is 2.1cm (considering the thickness of the origami hardboard is 0.1cm).

The simulated results of the acoustic intensity distribution at a frequency of 3700Hz (an optimized frequency for sound focusing related to the structural size) is shown in Fig. 2(e), in which the acoustic focusing effect is clearly observed. In experiment, the sound sources are set as five smaller loudspeakers (diameter=2cm) at five exits as the arrows illustrated in Fig. 2(b). The corresponding measured results are obtained by scanning the acoustic field in the given region (24cm×36cm region, marked by dashed square in the figure). The measured result in the inset of Fig. 2(e) agrees well with the simulated one, and shows a clear obtained focusing effect. Figure 2(f) shows the simulated (Simu.) and the experimental (Expt.) acoustic intensity distributions at the coordinate of x=34cm (marked by dashed white line) for 3700Hz. The experimental result agrees well with the simulated one, demonstrating a good focusing effect. It is noted that larger arrays (6×7 and 8×9) can be also designed for acoustic focusing, which are numerically shown in Appendix A.
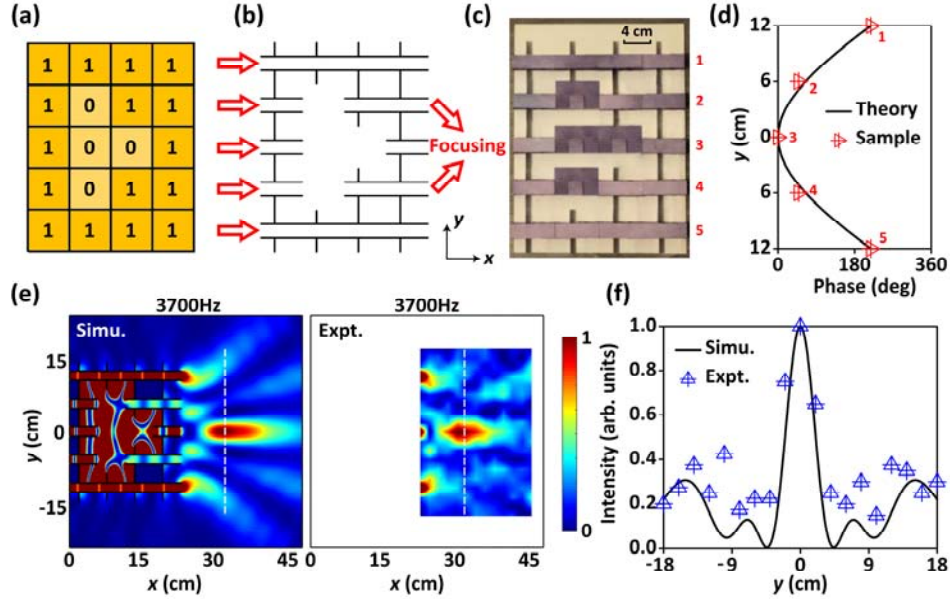
FIG. 2. The designed origami metamaterial for the acoustic focusing. (a) The array consists of a specific distribution of State #1 and State #0. (b) The 2D structure and model of the array. The arrows indicate incident and transmitted directions (c) A photograph of the fabricated metamaterial. A scale bar is shown in the figure. (d) Schematic diagram of the phase profile for acoustic focusing.

(e) The simulated and the measured acoustic intensities of the acoustic focusing at the frequency of 3700Hz. (f) The simulated (Simu.) and the experimental (Expt.) acoustic intensity distributions at the coordinate of x=34cm (marked by dashed white line in (d)) for 3700Hz.

B. Acoustic beam splitting

Figure 3 provides the design of the conceived metastructure for the acoustic beam splitting [26]. We have used the same states of the unit cells (*viz.*, State #1 and State #0) and the same sound source as acoustic focusing to realize the acoustic beam splitting. As shown in Figs. 3(a-d), the gradient profile for acoustic splitting is inversed compared with acoustic focusing, since the

designed phase profile at the output interface is inversed ($\phi = 2\pi - k(\sqrt{y_0^2 + 0.01} - 0.1)$) as shown in Fig. 3(d).

Figure 3(e) illustrates the simulated and experimental results of the acoustic splitting. Acoustic pressure amplitude at 3700Hz is shown in the figure, in which the acoustic wave is split into two parts with approximately ±45° directions. The acoustic fields are considered at the suitable region (24cm×36cm region, marked by square in the figure), evidencing a good agreement between the measured acoustic field and the simulated acoustic pressure distribution. Figure 3(f) shows the simulated (Simu.) and the experimental (Expt.) results of wave directivity at a frequency of 3700Hz. The directivity is measured at far-field regime (scanning from -90° to +90°). The simulated and the experimental results show that the sound energy is mainly directed at ±45° angles, which is consistent with the results of the wave field distribution in Fig. 3(e).
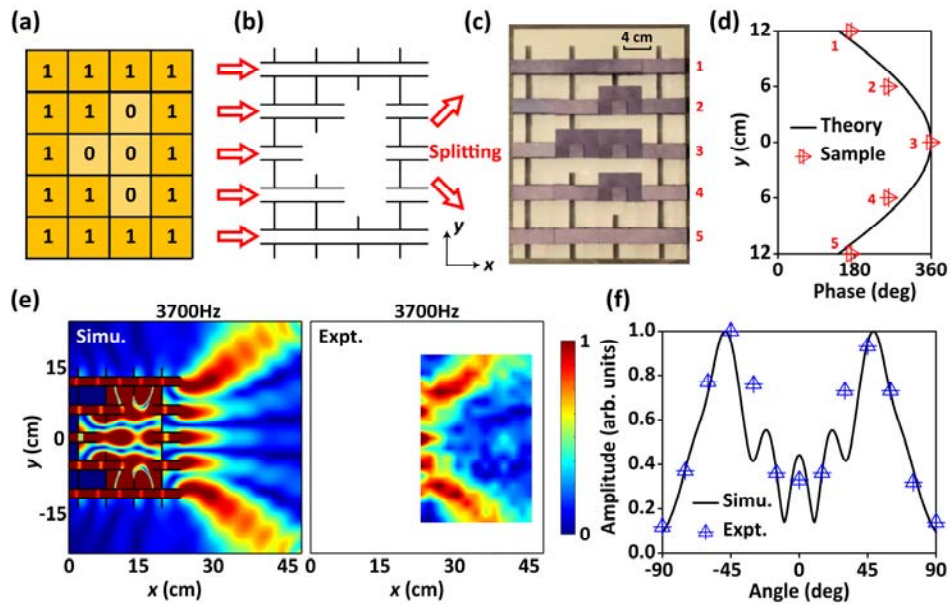
FIG. 3. The design of the acoustic beam splitting. (a) The array consists of State #1 and State #0. (b) The 2D structure and model of the array. (c) The photograph of the conceived metamaterial.

A scale bar is shown in the figure. (d) Schematic diagram of the phase profile for acoustic beam splitting. (e) The simulated and the measured acoustic pressure of the acoustic splitting at 3700Hz. (f) The simulated (Simu.) and the experimental (Expt.) directivity show that the sound energy are mainly at directed with ±45° angles.

C. Acoustic localization

On the other hand, we have investigated the sound localization effect. Figure 4 shows the demonstration of the acoustic localization [27] using a specific design of our origami metamaterial. The array consists of State #2 and State #0. State #2 has four exits in x-y plane that has higher degree of freedom than State #1. One unit in the array is set as State #0, which acts as a defect for the acoustic localization as shown in Figs. 4(a-c). The latter can be explained by the fact that the size of the cavity defect matches with the involved wavelength. Figure 4(d) shows the eigenmodes for a 3×3 supercell with a defect. The eigenmodes at 819Hz has sound localization effect in the defect. Other eigenmodes at 1418Hz and 1616Hz has sound distributed in the channels instead of the defect. These results suggest that the wave around the frequency of 819Hz is coupled to the defect, which can be analytically obtained from the resonant frequency of the Helmholtz resonator [30]:

$$ f = \frac{c_0}{2\pi}\sqrt{\frac{S}{LV}}, \qquad (2) $$

where $S=a^2$ is the area of the neck, $L=a$ is the length of the neck, and $V \approx a(b-a)^2$ is the volume of the cavity. Thus, the resonant frequency for the cavity is approximately as $f=c_0/2\pi(b-a)$.

On the other hand, the eigenfrequency for a 4×5 supercell is 655Hz (see Appendix C). Due

to the coupling effect, it is lower than the eigenfrequency of 819Hz for a 3×3 supercell. Thus, the working bandwidth is around these two eigenfrequencies (655Hz and 819Hz). We can, then, achieve acoustic localization within the frequency range of 600~800Hz. In experiment, the wave is incident from the specific unit cell as shown by the arrow marked in Fig. 4(b). Fig. 4(e) shows the simulated result of the acoustic pressure amplitude distribution at 700Hz, in which the acoustic localization at the defect is observed. In order to experimentally demonstrate the localization effect, we have measured two positions in the array, marked by "A" and "B", respectively, in Figs. 4(c) and 4(e). The larger acoustic amplitude at point A than at point B means that the acoustic localization occurs. Figure 4(f) shows the simulated and the measured acoustic amplitude at points A and B within the frequency range of 500~800Hz. The simulated and measured amplitudes at point A are 20 times and 11 times larger than the ones at point B at 700Hz, respectively. The apparent contrast of the two values demonstrates the acoustic localization effect.
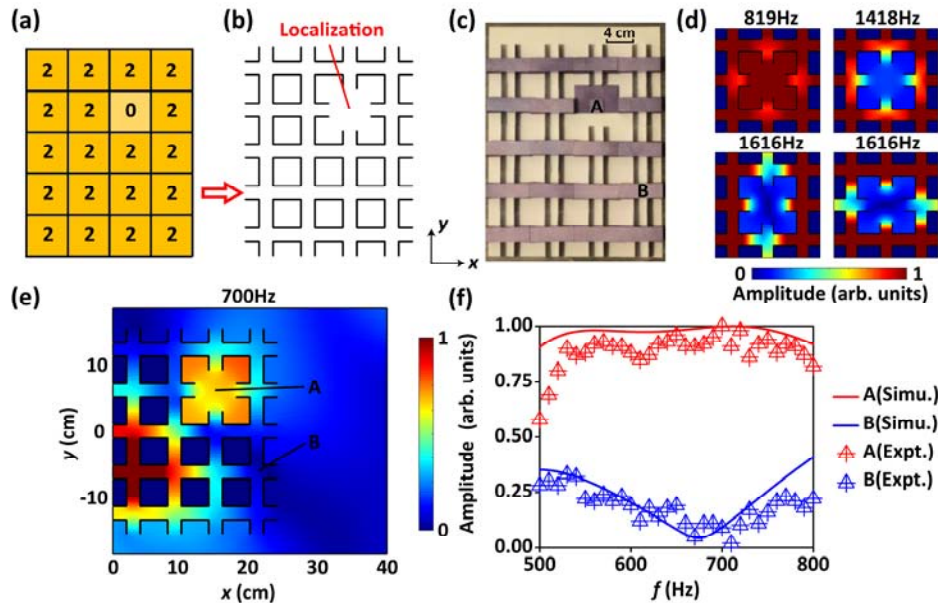
FIG. 4. The design of the acoustic localization. (a) The array consists of State #2 and State #0. (b)

The 2D structure and model of the array. (c) The photograph of the sample. A scale bar is shown in the figure. (d) Eigenmodes for a 3×3 supercell with a defect. (e) The simulated and the measured acoustic pressure amplitude of the acoustic localizations at 700Hz. The positions of "A" and "B" are measured, respectively. (f) The simulated (Simu.) and the experimental (Expt.) acoustic pressure amplitude within 500~800Hz at points A and B, respectively.

D. Acoustic one-way transmission

The one-way transmission of sound waves which is of tremendous interest on scientific and engineering aspects has been also investigated. Figure 5 shows the proposed design of the acoustic one-way transmission [28]. As shown in Figs. 5(a-c), the array consists of State #2, State #3, and State #0, respectively. State #3 is introduced at the upper and bottom boundaries of the array. The incidences are set as plane wave from left side (defined as positive incidence (PI)) and right side (defined as negative incidence (NI)), respectively. As shown in Figs. 5(a-c), the designed profile of different states breaks the spatial inversion symmetry in the 4×5 array. The asymmetric effects can be explained, then, by asymmetric wave vector conversion for two opposite incident directions [28]. As schematically shown in Fig. 5(d), the periodic structure acts as a spatial filter for different wave modes, which blocks the NI wave, while the diffraction structure causes the spatial modes transition for PI wave to pass the whole structure. (see details and mechanism in Appendix D)

Figure 5(e) shows the simulated acoustic pressures at 2150Hz for PI and NI, respectively. The results show that the acoustic wave can pass through the structure from PI direction, but cannot pass through it from NI direction, exhibiting the one-way transmission effect. It is noted that the propagating direction of transmitted wave for PI has been changed due to the reciprocity

principle in such a linear system [29]. In experiment, a loudspeaker is fixed 1m away from the surface of the sample to mimic plane wave incidence. Figure 5(e) shows the simulated and measured transmissions (defined as the sound power at the cross-section of the sample) within the frequency range of 2000~2300Hz. The results evidence that the simulated and measured transmissions from PI direction is 18 times and 13 times larger than the ones from NI direction at 2150Hz. This demonstrates the one-way acoustic transmission effect produced by the proposed origami-inspired metamaterial. It is worth mentioning that, the operation frequency (2150Hz) of acoustic one-way transmission is lower than the operation frequency (3700Hz) of acoustic focusing and splitting. This is due to that for a fixed geometry and diffraction pattern (see Appendix D, the interface between diffraction structure and the periodic structure is the same as the interfaces of acoustic focusing and splitting), incident wave with a smaller wave number (a lower frequency) will be easier to be converted to higher order modes.
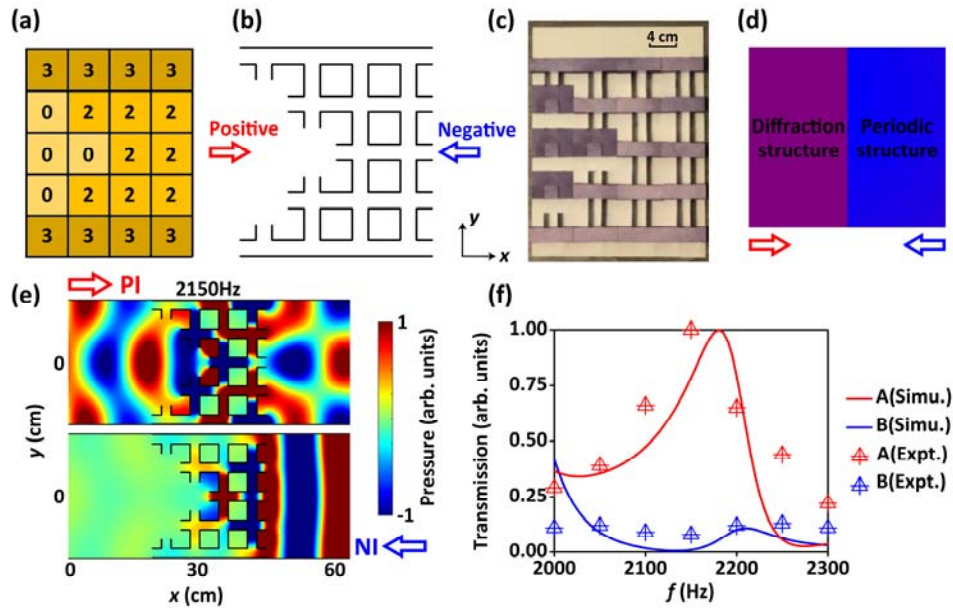
FIG. 5. The design of the one-way acoustic transmission. (a) The array consists of State #2, State #3, and State #0. (b) The 2D structure and model of the array. (c) The photograph of the origami

sample. A scale bar is shown in the figure. (d) Schematic diagram of the one-way acoustic transmission structure. (e) The simulated and the acoustic pressure of the one-way transmission at 2150Hz from positive incidence (PI) and negative incidence (NI). (f) The simulated (Simu.) and the experimental (Expt.) transmissions for PI and NI, respectively, within 2000~2300Hz. The transmission is defined as the sound power at the cross-section of the origami sample.

IV. CONCLUSION

In summary, we have provided the design of a reconfigurable origami-inspired metamaterial with various tailored functionalities, including acoustic focusing, beam splitting, localization and one-way transmission. In each design, we have used combinations of different states of tunable origami-based unit cells to demonstrate numerically and experimentally specific functionalities. We have explored the sound wave manipulation ability of origami-inspired metamaterials, presenting simple configuration, tunable structure, multifunctionality, and light weight. The novelty of our findings paves the way towards an alternative approach for controllable sound wave manipulation by origami-inspired metamaterials. This can lead to pragmatic applications, such as noise control and sound field control.

APPENDIX A: DETAILS FOR ACOUSTIC FOCUSING

The acoustic focusing can be also designed in a larger array, by the optimization of the distributions of State #1 and State #0. Figure 6 shows the designs and the simulations for the 4×5

array, 6×7 array and 8×9 array with the focal distance 10cm, 15cm and 10cm, respectively.
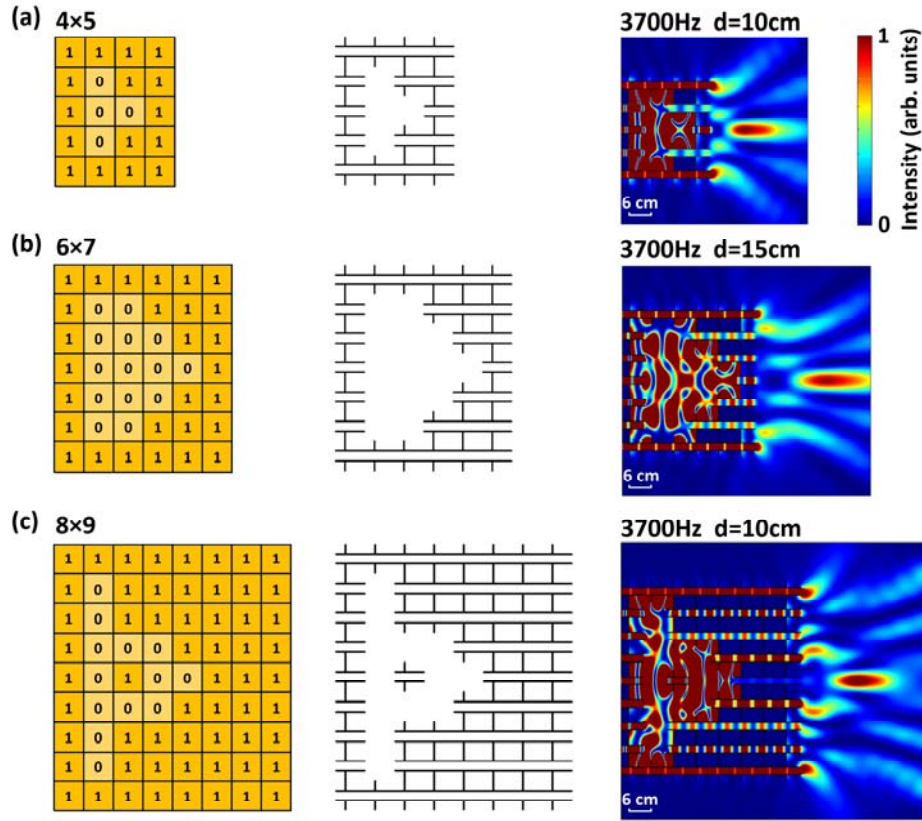
FIG. 6. Simulations of large array for acoustic focusing (a) The simulation for 4×5 array. The focal distance is 10cm. (b) The simulation for 6×7 array. The focal distance is 15cm. (c) The simulation for 8×9 array. The focal distance is 10cm.

The acoustic focusing design requires specific phase profiles at the exit of the array, which is based on the phase shift difference between the narrow channels (States #1) and the cavities (formed by several States #0). The phase shift of the narrow channel is mainly decided by its total length. The structure of States #0 combining with surrounded States #1 can form a large cavity. Acoustic resonances inside the cavity and the diffraction at the opening of the channel will influence the phase shift for the transmitted wave. Figure 7 shows the phase diagram of

acoustic focusing for a 8×9 array. The 2D structure is shown in Figs. 7(a) and 7(b). In the simulation, we set 8 probe lines from $x=0$cm to $x=42$cm (with a step of 6cm) to detect the acoustic wave phase. The simulated acoustic intensity distribution with focal distance of 10cm is shown Fig. 7(c). Figure 7(d) shows the simulated acoustic wave phase distribution. The detected acoustic wave phases at 8 probe lines are displayed in Fig. 7(e), which clearly shows the phase changes at each unit cell in the array. The phases at $x=42$cm agree well with the theory values $\phi = k(\sqrt{y_0^2 + 0.01} - 0.1)$ for acoustic focusing with focal distance 10cm. The red dashed rectangles marks where the phase shifts are very large, which corresponding to the cavities in the structure formed by several States #0 surrounded by States #1. The results suggest that the designed cavities have obviously different phase shifts from the narrow channels. The phase shift of the arrow is mainly decided by the length, but the phase in designed cavity is influenced by acoustic resonances inside and the diffraction at the opening of the channel. Thus, the distributions of States #1 and States #2 are optimized to achieve precise phase profile at the exit.
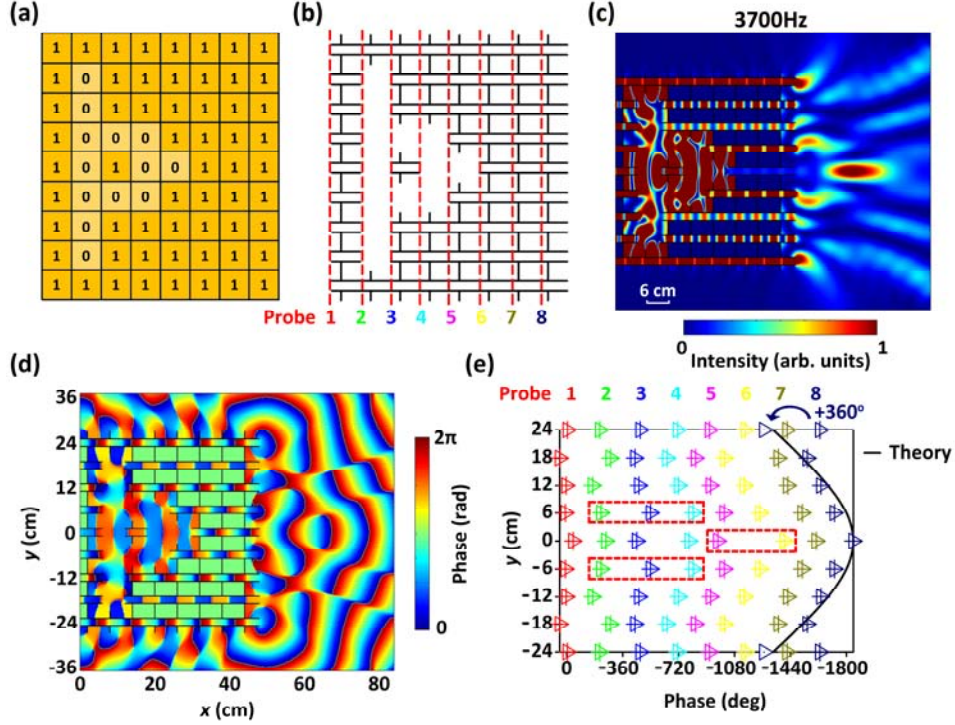
FIG. 7. The phase diagram of acoustic focusing for 8×9 array. (a) The array consists of a specific distribution of State #1 and State #0. (b) The 2D structure and model of the array. 8 probe lines are set (with a step of 6cm) to detect the acoustic wave phase. (c) The simulated acoustic intensity distribution. The focal distance is 10cm. (d) The simulated acoustic wave phase distribution. (e) The detected acoustic wave phases at 8 probe lines.

APPENDIX B: DETAILS OF NUMERICAL SIMULATIONS

Our design uses hardboard as the origami material whose acoustic impedance is much larger than the air background medium. We show the simulation results for different functionalities under three conditions for a comparison: 1. Setting hardboard as a hard boundary. 2. Setting hardboard as acoustic medium with the density of $\rho_1=1200kg/m^3$ and the sound speed of $c_1=500m/s$. 3. Setting hardboard as elastic medium with density of $\rho_1=1200kg/m^3$, Young's modulus of $E=5\times10^8Pa$, and Poisson's ratio of $\mu=0.33$. Figures 8(a-d) show that the acoustic

fields of focusing, splitting, localization, and one-way transmission for the three conditions are similar. These results validate that the elastic medium hardboard can be approximated to acoustic medium or hard boundary in simulations.
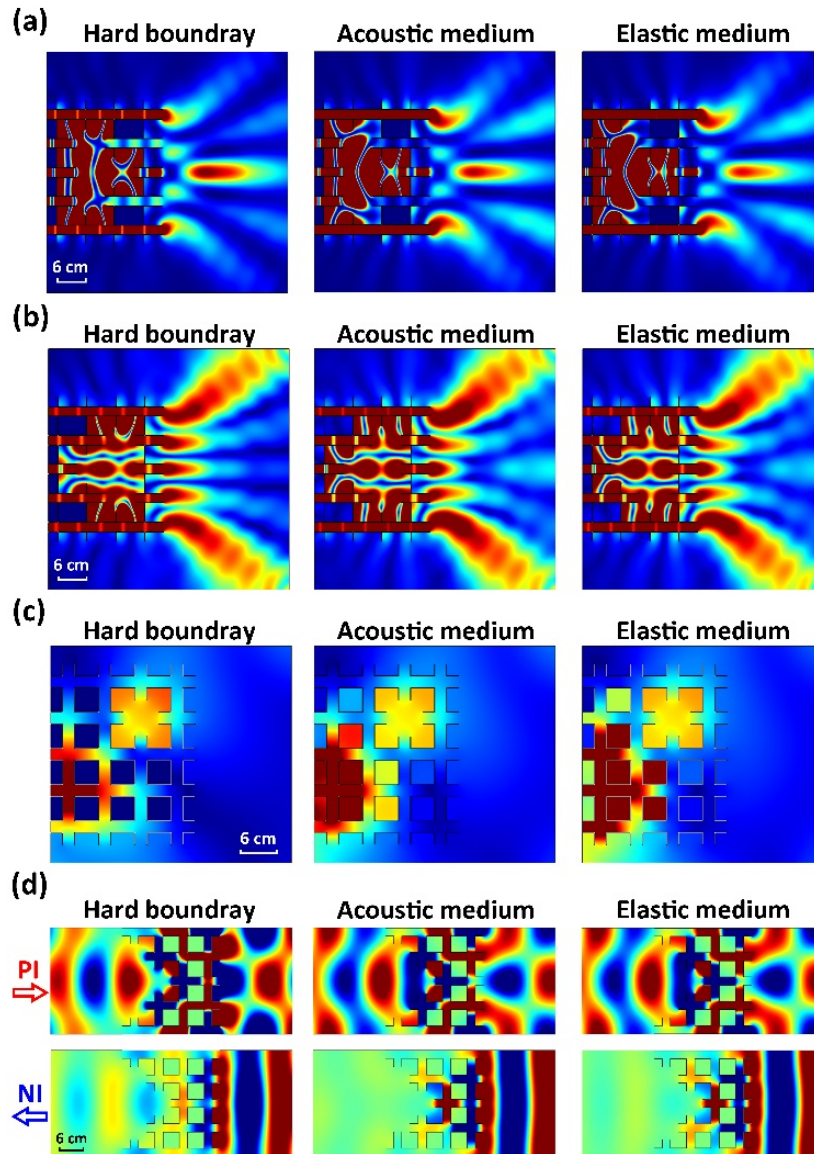
FIG. 8. (a) The simulation of acoustic focusing by setting the hardboard as hard boundary, acoustic medium and elastic medium, respectively. (b-d) The corresponding results for acoustic splitting, acoustic localization, and one-way sound transmission.

APPENDIX C: DETAILS FOR ACOUSTIC LOCALIZATION

Figure 9 shows the six eigenmodes of the 4×5 array with defect for acoustic localization. The localization at the defect appears at the eigenfrequency of 655Hz. It is noted that, in Fig. 4(d) of the main text, the eigenmode for acoustic localization of 3×3 array is at 819Hz. This difference is due to the coupling of all unit cells of the array, and will influence the resonant frequency. Thus, the acoustic localization effect in Fig. 4(f) is observed around these two eigenfrequencies. The bandwidth is from about 600Hz to 800Hz.
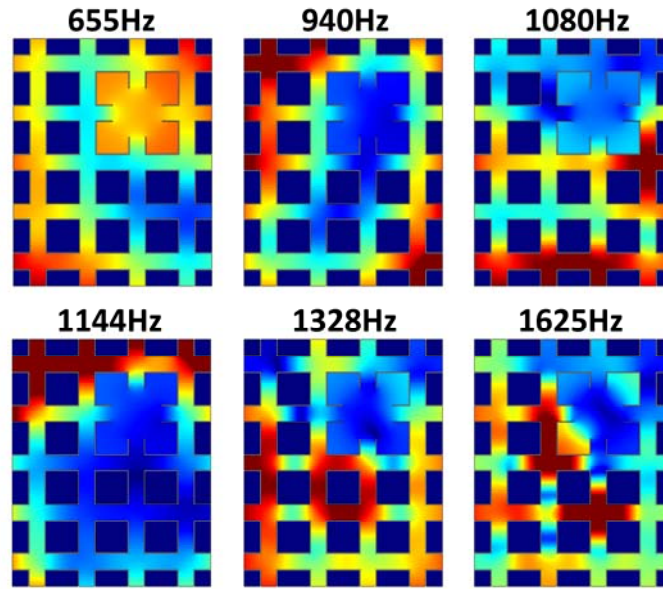
FIG. 9. Eigenmodes of the 4×5 array for acoustic localization. The localization at the defect appears at the eigenmode of 655Hz.

APPENDIX D: DETAILS FOR ACOUSTIC ONE-WAY TRANSMISSION

Figure 10 shows the design details for acoustic one-way transmission. Figure 10(a) displays the 2D structure of the array, while figure 10(b) exhibits the schematic diagram of the one-way

acoustic transmission structure consisting of diffraction structure and periodic structure. As shown in Fig. 10(c), the periodic structure acts as a spatial filter for different wave modes, which blocks the NI wave, while the diffraction structure acting as a converter causes the spatial modes transition for PI wave to pass the whole structure. In Fig. 10(d), the simulated acoustic pressure field clearly shows that the diffraction structure can convert the transmitted wave into high-order mode as marked by black arrows, different from the periodic structure.
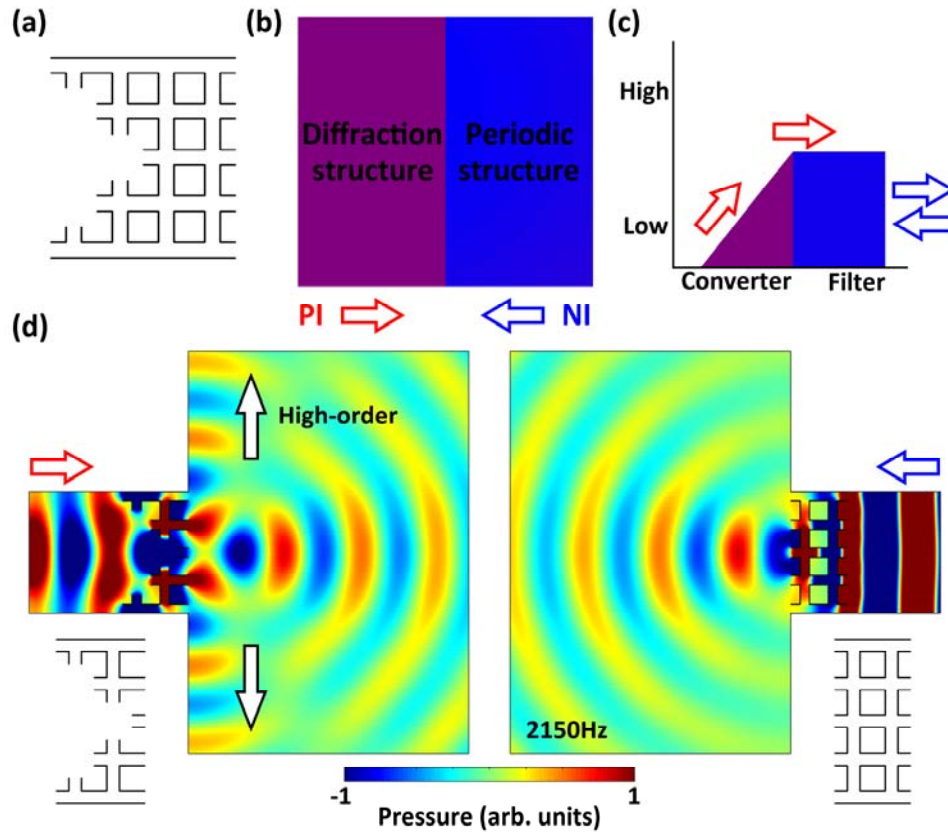
FIG. 10. The mechanism of one-way transmission. (a) The 2D structure and model of the array. (b) Schematic diagram of the one-way acoustic transmission structure. (c) The periodic structure acts as a filter, while the diffraction structure acts as a converter. (d) The simulated transmitted acoustic pressure fields for diffraction structure and periodic structure, respectively.

References

[1]   J. O'Rourke, How to Fold It: The Mathematics of Linkages, Origami and Polyhedra, (Cambridge Univ. Press, 2011).

[2]   P. Wang-Iverson, R. J. Lang, and Y. Mark, Origami 5: Fifth International Meeting of Origami Science, Mathematics, and Education, (CRC Press, 2011).

[3]   K. Bertoldi, V. Vitelli, J. Christensen, and M. Van Hecke, Flexible mechanical metamaterials, Nat. Rev. Mater. **2**, 17066 (2017).

[4]   M. Schenk and S. D. Guest, Geometry of Miura-folded metamaterials, Proc. Natl. Acad. Sci. U.S.A. **110**, 3276-3281 (2013).

[5]   Z. Y. Wei, Z. V. Guo, L. Dudte, H. Y. Liang, and L. Mahadevan, Geometric mechanics of periodic pleated origami, Phys. Rev. Lett. **110**, 215501 (2013).

[6]   M. Eidini, and G. H. Paulino, Unraveling metamaterial properties in zigzag-base folded sheets. Sci. Adv. **1**, e1500224 (2015).

[7]   J. L. Silverberg, J. H. Na, A. A. Evans, B. Liu, T. C. Hull, C. D. Santangelo, R. J. Lang, C. Hayward, and I. Cohen, Origami structures with a critical transition to bistability arising from hidden degrees of freedom, Nat. Mater. **14**, 389–393 (2015).

[8]   S. Waitukaitis, R. Menaut, B. G. Chen, and M. van Hecke, Origami multistability: From single vertices to metasheets, Phys. Rev. Lett. **114**, 055503 (2015).

[9]   H. Yasuda and J. Yang, Reentrant origami-based metamaterials with negative Poisson's ratio and bistability, Phys. Rev. Lett. **114**, 185502 (2015).

[10]   P. P. Pratapa, K. Liu, and G. H. Paulino, Geometric Mechanics of Origami Patterns Exhibiting Poisson's Ratio Switch by Breaking Mountain and Valley Assignment. Phys. Rev. Lett. **122**, 155501 (2019).

[11]   B. G.. Chen, B. Liu, A. A. Evans, J. Paulose, I. Cohen, V. Vitelli, and C. D. Santangelo, Topological mechanics of origami and kirigami, Phys. Rev. Lett. **116**, 135501 (2016).

[12]   J. L. Silverberg, A. A. Evans, L. McLeod, R. C. Hayward, T. Hull, C. D. Santangelo, and I. Cohen, Using origami design principles to fold reprogrammable mechanical metamaterials, Science **345**, 647–650 (2014).

[13]   S. Li, H. Fang, and K. W. Wang, Recoverable and programmable collapse from folding pressurized origami cellular solids, Phys. Rev. Lett. **117**, 114301 (2016).

[14]   S. Felton, M. Tolley, E. Demaine, D. Rus, and R. Wood, A method for building self-folding machines, Science **345**, 644-646 (2014).

[15]   D. Rus, and M. T. Tolley, Design, fabrication and control of origami robots, Nat. Rev. Mater. **3**, 101–112 (2018).

[16] Z. M. Song, T. Ma, R. Tang, Q. Cheng, X. Wang, D. Krishnaraju, R. Panat, C. K. Chan, H. Y. Yu, and H. Q. Jiang, Origami lithium-ion batteries, Nat. Commun. **5**, 3140 (2014).

[17] E. Boatti, N. Vasios, and K. Bertoldi, Origami metamaterials for tunable thermal expansion. Adv. Mater. **29**, 1700360 (2017).

[18] L. Z. Xu, T. C. Shyu, and N. A. Kotov, Origami and kirigami nanocomposites, ACS Nano **11**, 7587-7599 (2017).

[19] P. M. Reis, F. L. Jiménez, and J. Marthelot, Transforming architectures inspired by origami, Proc. Natl. Acad. Sci. U.S.A. **112**, 12234-12235 (2015).

[20] J. T. B. Overvelde, T. A. de Jong, Y. Shevchenko. S. A. Becerra, G. M. Whitesides, J. C. Weaver, C. Hoberman, and K. Bertoldi, A three-dimensional actuated origami-inspired transformable metamaterial with multiple degrees of freedom, Nat. Commun. **7**, 10929 (2016).

[21] S. Babaee, J. T. B. Overvelde, E. R. Chen, V. Tournat, and K. Bertoldi, Reconfigurable origami-inspired acoustic waveguides, Sci. Adv. **2**, e1601019 (2016).

[22] S. A. Cummer, J. Christensen, and A. Alu, Controlling sound with acoustic metamaterials. Nat. Rev. Mater. **1**, 16001 (2016).

[23] G. C. Ma and P. Sheng, Acoustic metamaterials: From local resonances to broad horizons. Sci. Adv. **2**, e1501595 (2016).

[24] B. Assouar, B. Liang, Y. Wu, Y. Li, J. C. Cheng, and Y. Jing, Acoustic metasurfaces, Nat. Rev. Mater. **3**, 460–472 (2018).

[25] X. D. Fan, Y. F. Zhu, B. Liang, J. Yang, and J. C. Cheng, Broadband convergence of acoustic energy with binary reflected phases on planar surface, Appl. Phys. Lett. **109**, 243501 (2016).

[26] Y. N. Guo, D. Brick, M. Großmann, M. Hettich, and T. Dekorsy, Acoustic beam splitting at low GHz frequencies in a defect-free phononic crystal, Appl. Phys. Lett. **110**, 031904 (2017).

[27] J. Zhu, Y. Chen, X. Zhu, F. J. Garcia-vidal, X. Yin, W. Zhang, and X. Zhang, Acoustic rainbow trapping, Sci. Rep. **3**, 1728 (2013).

[28] X. F. Li, X. Ni, L. Feng, M. H. Lu, C. He, and Y. F. Chen, Tunable unidirectional sound propagation through a sonic-crystal-based acoustic diode, Phys. Rev. Lett. **106**, 084301 (2011).

[29] Y. F. Zhu, X. Y. Zou, B. Liang, and J. C. Cheng, Acoustic one-way open tunnel by using metasurface, Appl. Phys. Lett. **107**, 113501 (2015).

[30] L. Kinsler, Fundamentals of Acoustics (Wiley, New York, 1982).